PAPER

# Spinodal de-wetting of light liquids on graphene

IOP Publishing Journal of Physics: Condensed Matter
J. Phys.: Condens. Matter **34** (2022) 175001 (11pp) https://doi.org/10.1088/1361-648X/ac4f7e

# Spinodal de-wetting of light liquids on graphene

**Juan M Vanegas[1], David Peterson[1], Taras I Lakoba[2] and Valeri N Kotov[1,*]**

[1] Department of Physics, University of Vermont, Burlington, VT 05405, United States of America
[2] Department of Mathematics and Statistics, University of Vermont, Burlington, VT 05405, United States of America

E-mail: valeri.kotov@uvm.edu

Received 5 December 2021, revised 22 January 2022
Accepted for publication 27 January 2022
Published 25 February 2022

**Abstract**

We demonstrate theoretically the possibility of spinodal de-wetting in heterostructures made of light–atom liquids (hydrogen, helium, and nitrogen) deposited on suspended graphene. Extending our theory of film growth on two-dimensional (2D) materials to include analysis of surface instabilities via the hydrodynamic Cahn–Hilliard-type equation, we characterize in detail the spatial and temporal scales of the resulting spinodal de-wetting patterns. Both linear stability analysis and direct numerical simulations of the surface hydrodynamics show micron-sized (generally material dependent) patterns of 'dry' regions. The physical reason for the development of such instabilities on graphene can be traced back to the inherently weak van der Waals interactions between atomically thin materials and atoms in the liquid. Thus 2D materials could represent a new theoretical and technological platform for studies of spinodal de-wetting.

Keywords: graphene, spinodal de-wetting, 2D materials, surface instabilities, thin liquid films, van der Waals systems

(Some figures may appear in colour only in the online journal)

## 1. Introduction

One of the greatest developments in condensed matter physics in the last two decades has been the discovery of novel two-dimensional (2D), atomically thin materials, such as graphene [1]. Numerous 2D materials structurally similar to graphene also exist, for example the large family of transition-metal dichalcogenides (e.g., $MoS_2$). These can form the building blocks of the so-called VDW heterostructures [2, 3]. Van der Waals (VDW) forces control a wide variety of phenomena in nature as they represent interactions between neutral bodies. Such interactions depend on the polarizability of individual atoms and materials and therefore are sensitive to the geometry and screening of the Coulomb force which is ultimately responsible for the VDW interaction [4]. VDW interactions can play an especially important role near surfaces where they control wetting phenomena of liquids deposited on materials, contact angles, as well as pattern formation instabilities, such as spinodal de-wetting [5–8].

There are several important features of 2D materials that make them uniquely attractive candidates for studies of liquid adsorption, wetting and related VDW-driven phenomena. (1) First, the polarization function of 2D materials can be calculated with great accuracy. This in turn leads to an excellent description of VDW forces. (2) Moreover, the polarization of graphene reflects its characteristic Dirac-like electronic dispersion which can be controlled by external factors such as application of mechanical strain [9–11], change in the chemical potential (addition of carriers) [1, 12], change in the dielectric environment (i.e., presence of a dielectric substrate affecting screening), etc. This means that VDW-related properties can be in principle effectively manipulated. (3) Also, being purely

* Author to whom any correspondence should be addressed.

 

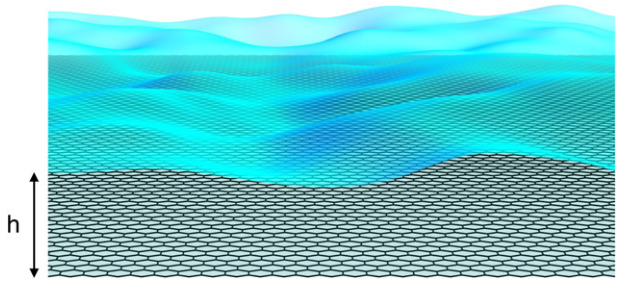


**Figure 1.** Liquid film of thickness $h$ formed on suspended graphene.

2D structures, materials like graphene can be engineered and arranged in various configurations. For example, the authors of reference [13] considered three configurations, where the graphene sheet is either suspended in vacuum, or is submerged in the liquid, or rests on a bulk substrate. From the point of view of the present work, the possibility to have the suspended configuration, shown in figure 1, is the most important one. In this configuration, where only a single sheet of (carbon) atoms exerts a relatively weak VDW force on the atoms of the film, spinodal de-wetting patterns can form on the film surface. It is important to note that despite having atomic thickness, graphene is known to be generally impermeable even to small atoms [14–17]; hence the liquid film will remain on that side of the sheet where it was initially present.

The purpose of the present work is to study in detail the main characteristic scales of the surface spinodal patterns for three light elements: He, $H_2$, and $N_2$, forming a liquid layer on top of suspended graphene. The phenomenon of spinodal de-wetting itself has a long history [18] (prior to that, a mathematically equivalent analysis of spontaneous rupture of a free film was done in [19]) and has been theoretically predicted and detected in numerous situations involving polymers, liquid metals, etc; see, e.g., [6, 8, 20–31]. This type of de-wetting and the corresponding description bears much conceptual and technical similarity to spinodal decomposition which describes phase separation, commonly modeled via the Cahn–Hilliard equation (CHE) [32]. The main equation governing the evolution of the film thickness, that describes spinodal decomposition (the analog of the CHE in this case), appears in the original literature [19]. We will use the formulation [22] which adopts the notion of disjoining pressure $\Pi(h)$, where $h$ is the (local) thickness of the liquid film. The shape of $\Pi(h)$, which is representative for all cases considered in this work, is shown in figure 2. For those values $h$ where this graph has a positive slope, an instability of the film's flat surface to small fluctuations is favored, which eventually leads to the film breakup and formation of spinodal de-wetting patterns. A feature of the graph $\Pi(h)$ that guarantees the existence of the region with $\mathrm{d}\Pi(h)/\mathrm{d}h > 0$ (for $h > h^*$; see figure 2) is the existence of a critical value $h_c$ where $\Pi(h)$ changes sign.

In order to calculate $\Pi(h)$, we rely on a previous work [13], where we present a detailed description of the graphene–liquid–vapor configuration. (The analysis of that work is also applicable to any atomically thin 2D material with liquid on top.) It is based on the Dzyaloshinskii–Lifshitz–Pitaevskii (DLP) theory [33, 34], which is the standard many-body approach for VDW forces in a three-layer (substrate–liquid–vapor) configuration with given dielectric functions. This approach provides a very reliable description, well verified by experiment for different substrates and liquids [4, 35]. The work [13] extends and modifies the original DLP approach, designed for bulk materials, to the case of 2D substrates such as graphene. For the suspended configuration in figure 1, it was noted in [13] that $\Pi(h)$ goes through zero at $h_c$ and $\mathrm{d}\Pi(h)/\mathrm{d}h > 0$ when $h > h^*$, for practically all 2D materials and atoms studied there. The values of $h_c$ and $h^*$ depend strongly on the type of liquid and 2D material substrate, but the existence of a region with $\mathrm{d}\Pi(h)/\mathrm{d}h > 0$ and hence, an instability of the film, appears to be generic to the suspended configuration. This should be contrasted with the case where a thin film of a light element (e.g., helium) is placed over most bulk materials (e.g., graphite) [36], as well as with the case of the other two configurations of the graphene sheet considered in [13] (i.e., where the sheet is either on a bulk substrate or submerged). In both of those cases, the attractive force of atoms inside the film to the substrate is greater than that between atoms inside the film, resulting in wetting behavior and stable film growth. Thus, the focus of the present work is on studying characteristic scales of spinodal de-wetting patterns over a suspended graphene sheet, which represents a unique configuration where an instability is guaranteed to occur.

The rest of the paper is organized as follows. In section 2 we present results for the disjoining pressure for three types of light liquids on graphene. In section 3 we analyze the surface hydrodynamics equation (CHE) and present results for the characteristic spinodal scales in the linear stability approximation. In section 4 we present brief details of the numerical method used to simulate the CHE and then provide a detailed description of the spinodal de-wetting pattern formation and evolution. Section 5 contains our conclusions. In appendix A we present details of the disjoining pressure calculation.

## 2. Disjoining pressure for light liquids on graphene

Our starting point is the analysis of reference [13], where the VDW interaction energy of the configuration in figure 1 was calculated. We consider three types of light atoms: He, $H_2$ and $N_2$. The energy is very sensitive to the atomic parameters, most notably the atomic polarizabilities, which are known quite accurately. The dynamical polarization of graphene is also well known and is an important ingredient of the calculation. For the purpose of studying the spinodal instability, it is convenient to introduce the disjoining pressure $\Pi(h)$, which is related to the derivative of the VDW energy as summarized in appendix A.

The form of $\Pi(h)$ is an important ingredient for all subsequent calculations. Based on our previous results [13], the function $\Pi(h)$ can be parameterized with high accuracy in the following way:

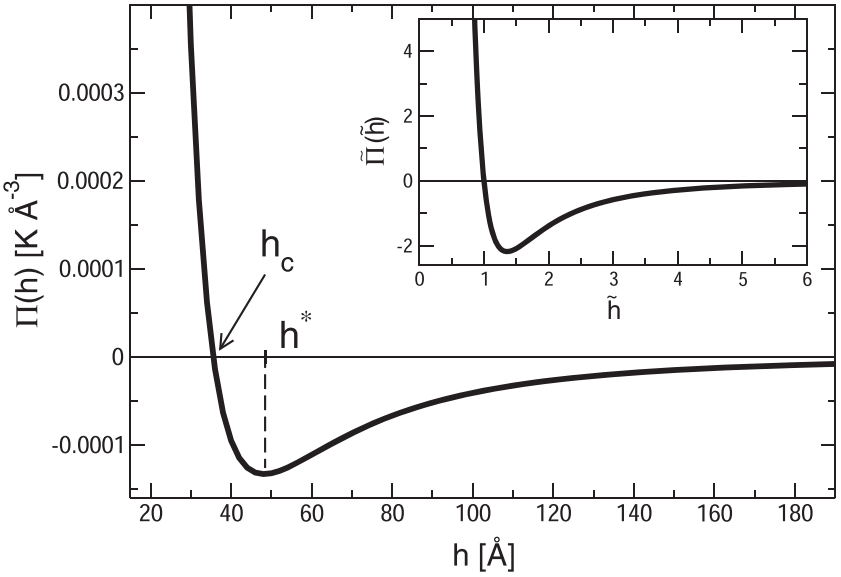


**Figure 2.** Disjoining pressure $\Pi(h)$ for $N_2$. Inset: dimensionless disjoining pressure as defined in the text, $\tilde{\Pi}(\tilde{h}) = \frac{\gamma^2}{\tilde{h}^3}\left(\frac{1-\tilde{h}}{\beta+\tilde{h}}\right)$, where $\tilde{h} = h/a$, and the notation $a \equiv h_c$ is defined in (2). The parameter $\beta = 0.37$, appropriate for $N_2$, and $\gamma = 5.13$ (see text).

$$\Pi(h) = \left\{-|\Pi_0| + \frac{\Pi_1}{h+L}\right\}\frac{1}{h^3} = \frac{|\Pi_0|}{h^3}\left(\frac{h_c - h}{h+L}\right). \quad (1)$$

The film thickness $h_c$ where $\Pi(h)$ changes sign, which from now we label as $a \equiv h_c$, depends on the parameters in the first part of the equation in the following way:

$$h_c = \frac{\Pi_1}{|\Pi_0|} - L \equiv a. \quad (2)$$

The crossover length $L$ is the characteristic length-scale which separates the $-1/h^3$ and $1/h^4$ behavior of $\Pi(h)$. As emphasized in [13] and appendix A, the existence of such a crossover is due to the fact that the dynamical polarization of graphene has a very strong momentum dependence, reflecting the motion of Dirac quasiparticles in the layer. The parameterization, equation (1) is convenient because it reflects the presence of two physically different parts with different signs: (a) the $\Pi_0$ term originates from the VDW interactions with the liquid itself (thus leading to negative pressure and tendency towards instability), and (b) the $\Pi_1$ term comes from the graphene–liquid interaction which favors positive pressure (and thus stable film growth). These two terms are written explicitly in terms of the VDW energies in appendix A. We also note that the derivation of $\Pi(h)$ was performed in the continuum limit, i.e., is valid for distances $h$ much larger than graphene's lattice spacing ($\sim$1 Å). In practice this means that such VDW calculations are typically used for $h \gtrsim 20$ Å where the corrugation of the surface is not important [10, 13].

Our fits for the values of the relevant parameters for the three types of atoms, as explained in appendix A, lead to the following results:

$$N_2: \quad |\Pi_0| = 72.8 \text{ K}, \quad \Pi_1 = 3592 \text{ K}\mathring{A}, \quad L = 13.3 \text{ Å},$$
$$\Rightarrow a = 36 \text{ Å} \quad (3)$$

$$H_2: \quad |\Pi_0| = 14.5 \text{ K}, \quad \Pi_1 = 1901 \text{ K}\mathring{A}, \quad L = 18.0 \text{ Å},$$
$$\Rightarrow a = 114 \text{ Å} \quad (4)$$

$$He: \quad |\Pi_0| = 2.09 \text{ K}, \quad \Pi_1 = 676 \text{ K}\mathring{A}, \quad L = 22.1 \text{ Å},$$
$$\Rightarrow a = 301 \text{ Å} \quad (5)$$

A representative plot of $\Pi(h)$ for $N_2$ is shown in figure 2. The minimum of $\Pi(h)$ occurs at a distance which we label as:

$$h^* = (2a - L + \sqrt{(2a-L)^2 + 9La})/3. \quad (6)$$

It is worth noticing that the values of the critical distance $a$ (as well as $h^*$) are quite different for the three elements. Armed with the precise form of $\Pi(h)$, equation (1), we proceed to study spinodal de-wetting pattern formation.

## 3. Surface hydrodynamics: Cahn–Hilliard equation and spinodal de-wetting instability

In this section we discuss the main equations of the theory and the linear stability analysis, appropriate for small initial perturbations of the surface. These are compared to numerical simulations based on the finite element method (FEM) which provide a complete solution and describe the full evolution in space and time.

### 3.1. Main equations

The equation describing the evolution of $h$ has the form [8, 19, 22]:

$$\partial_t h = \nabla \cdot \left\{\frac{h^3}{3\eta}\nabla\left(-\sigma\Delta h - \Pi(h)\right)\right\}. \quad (7)$$

This is the 2D analog of the CHE, which describes bulk phase separation. We use the standard notation:

$$h = h(x, y, t), \qquad \nabla = (\partial_x, \partial_y), \qquad \Delta = \nabla^2 = \partial_x^2 + \partial_y^2. \tag{8}$$

Here $(x, y)$ is the in-plane coordinate, $\eta$ is the liquid viscosity and $\sigma$ is the surface tension (between the liquid and its vapor). The first term on the right-hand side of (7) describes the resistance of the system to change of curvature (due to the Laplace pressure) and the second term is due to the disjoining pressure. This equation was derived in the assumption that there is no slippage between the film and the underlying substrate (i.e., graphene in this case). We estimated that the contribution of gravity to the evolution of films of sub-micron thickness, considered below, is negligible.

It is convenient to re-write the equation in dimensionless coordinates. First we observe that the following two dimensionless combinations can be constructed naturally

$$\alpha \equiv \frac{|\Pi_0|}{a^2\sigma}, \qquad \beta \equiv L/a\ . \tag{9}$$

Next, we choose to measure the height $h$ in units of the critical value $a$ and introduce new length and time scales $\xi, \tau$. The dimensionless height and space/time coordinates will be denoted by tilde:

$$\tilde{h} = h/a, \qquad \tilde{x} = x/\xi, \qquad \tilde{y} = y/\xi, \qquad \tilde{t} = t/\tau. \tag{10}$$

By substituting this form into the main equation we find that we can choose:

$$\xi = \frac{a\gamma}{\sqrt{\alpha}}, \qquad \tau = \frac{3\eta a}{\sigma}\frac{\gamma^4}{\alpha^2}, \tag{11}$$

where $\gamma$ is an arbitrary constant and will be commented on below. With these choices the original equation (7) becomes:

$$\partial_{\tilde{t}}\tilde{h} = \tilde{\nabla}\cdot\left\{\tilde{h}^3\tilde{\nabla}\left(-\tilde{\Delta}\tilde{h} - \tilde{\Pi}(\tilde{h})\right)\right\}, \quad \tilde{\Pi}(\tilde{h}) \equiv \frac{\gamma^2}{\tilde{h}^3}\left(\frac{1-\tilde{h}}{\beta+\tilde{h}}\right), \tag{12}$$

where $\tilde{\nabla} = (\partial_{\tilde{x}}, \partial_{\tilde{y}})$, $\tilde{\Delta} = \tilde{\nabla}^2$. A plot of $\tilde{\Pi}(\tilde{h})$ is shown in the inset to figure 2. By construction, $\tilde{\Pi}(\tilde{h})$ changes sign at $\tilde{h} = 1$.

### 3.2. *Summary of parameters for* $N_2$,$H_2$, He

In the following sections, we characterize the short and long time scale behavior of the CHE through linear stability analysis and numerical simulations. Therefore, we summarize here the relevant scales and physical parameters for different liquids:

$$\mathrm{N_2}: \beta = 0.37, \qquad a = 36\ \text{Å}, \qquad h^* = 49\ \text{Å},$$
$$\xi = 409\gamma\ \text{Å}, \qquad \tau = 4\gamma^4\ \mu\text{s} \tag{13}$$

$$\mathrm{H_2}: \beta = 0.16, \qquad a = 114\ \text{Å}, \qquad h^* = 153\ \text{Å},$$
$$\xi = 4116\gamma\ \text{Å}, \qquad \tau = 392\gamma^4\ \mu\text{s} \tag{14}$$

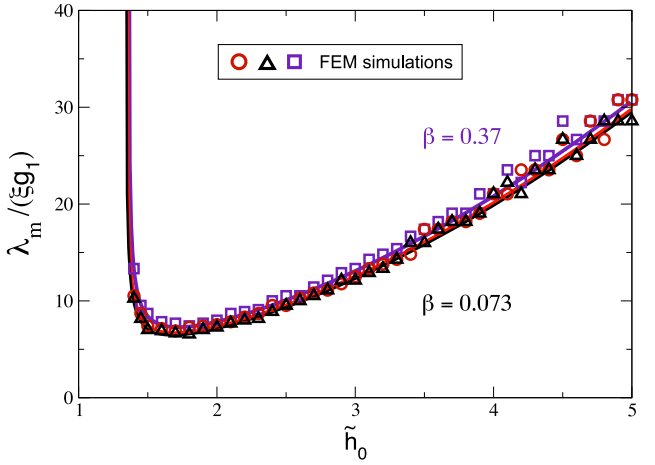


**Figure 3.** The dimensionless spinodal wavelength $\tilde{\lambda}_m = \lambda_m/\xi$, normalized to $g_1$ (see (20a)) versus the dimensionless uniform film height $\tilde{h}_0 = h_0/a$. For $\beta = 0.37$ (blue), the value for $N_2$, the onset of instability is at $\tilde{h}^* = 1.359$. For $\beta = 0.16$ (red), the value for $H_2$, the onset of instability is at $\tilde{h}^* = 1.346$. For $\beta = 0.073$ (black), the value for He, the onset of instability is at $\tilde{h}^* = 1.339$. Symbols correspond to values obtained from FEM simulations (section 4.1).

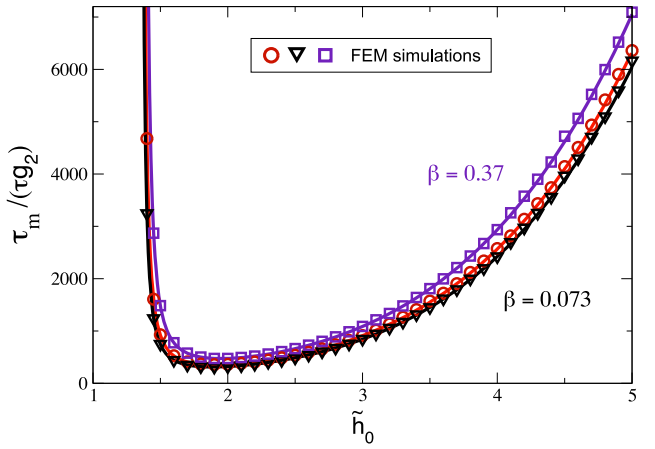


**Figure 4.** The dimensionless time constant characterizing spinodal growth, $\tilde{\tau}_m = \tau_m/\tau$ normalized to $g_2$ (see (20a)), versus the dimensionless uniform film height $\tilde{h}_0 = h_0/a$. The dependence on $\beta$ is more pronounced compared to the wavelength $\lambda_m$. Symbols correspond to values obtained from FEM simulations.

$$\mathrm{He}: \beta = 0.073, \qquad a = 301\ \text{Å}, \qquad h^* = 403\ \text{Å},$$
$$\xi = 27\,197\gamma\ \text{Å}, \qquad \tau = 75.5\gamma^4\ \text{ms} \tag{15}$$

For reasons explained in section 3.3, below we use $\gamma \approx 5.13$, so that $\gamma^4 \approx 693$. The values of $\beta, a, h^*$ are based on (3)–(6) and (9), while $\xi, \tau$ follow from (11) where the following values of the surface tension and viscosity are taken from standard tables and literature found in [37]. For $N_2$ at temperature 70 K, $\sigma = 10$ mN m$^{-1}$, $\eta = 220$ $\mu$Pa s; for $H_2$ at temperature 20 K, $\sigma = 2$ mN m$^{-1}$, $\eta = 13.5$ $\mu$Pa s; for He at temperature 2.5 K, $\sigma = 0.26$ mN m$^{-1}$, $\eta = 3.26$ $\mu$Pa s. The temperatures are chosen so that a liquid phase exists.

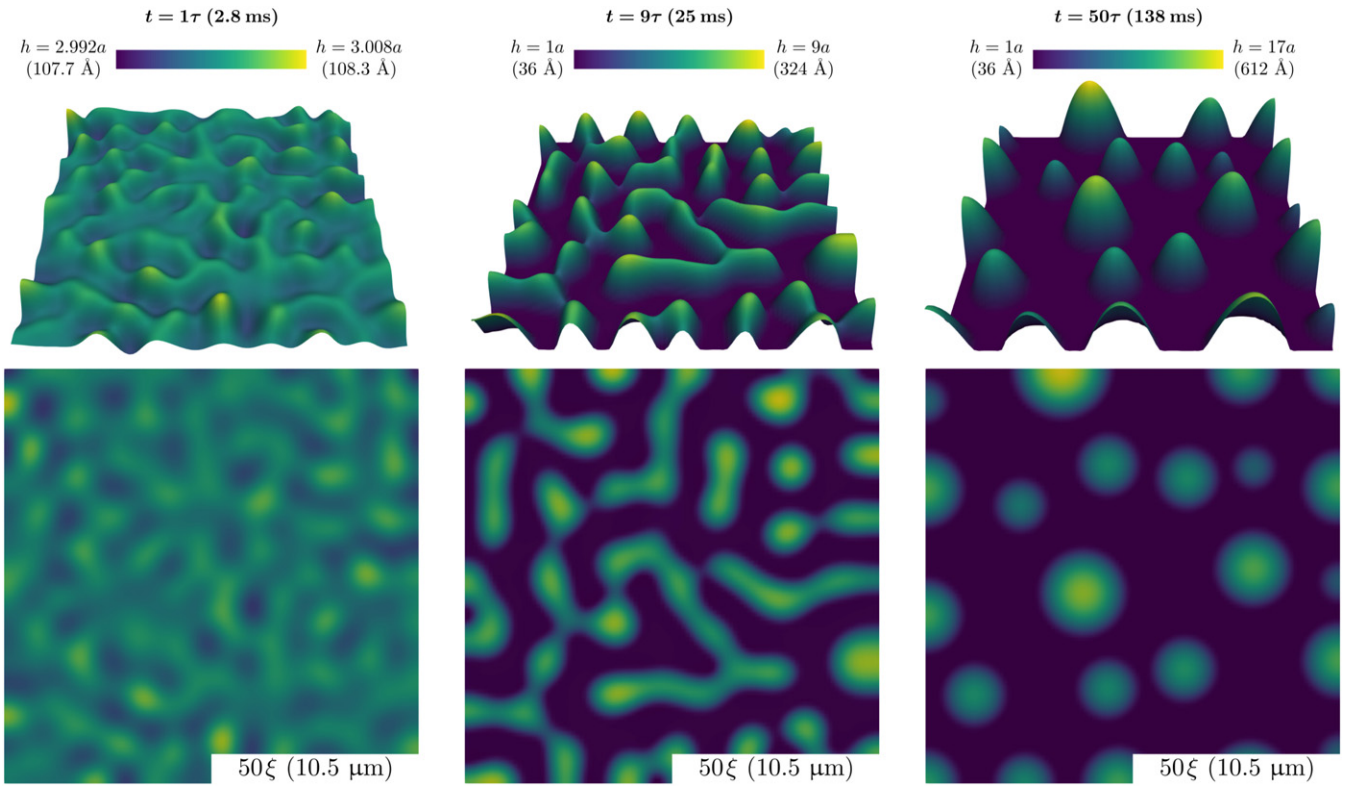


**Figure 5.** Spinodal de-wetting time evolution observed in FEM simulation of $N_2$ on graphene for a liquid of initially uniform height $\tilde{h}_0 = 3.0$ (with $\tilde{h}^* = 1.36$). During the initial stages of the simulation, the initial random variations ($<\tilde{h}_0 \times 10^{-5}$) lead to gradually increasing variations in the liquid height (left panel). These eventually form a well-defined spinodal de-wetting pattern (middle panel) where interconnected regions with excess liquid, $\tilde{h}(x, y) > \tilde{h}^*$, (light green/yellow colors) are surrounded by nearly flat regions with liquid height satisfying: $1 \lesssim \tilde{h}(x, y) < \tilde{h}^*$ (dark blue color). Note that the fact that $\tilde{h}(x, y) < \tilde{h}^*$ (as opposed to the two being equal) in the background regions is consistent with that reported in the literature; see, e.g., [25]. At long times, the regions of excess liquid continuously merge into distinct 'droplets' (localized regions of increased height).

We observe that the parameter $\beta$, which appears in equation (12), has quite different values depending on the type of liquid, although we find that the solution depends on $\beta$ relatively weakly. More importantly, the relevant length and time scales can differ by orders of magnitude.

### 3.3. Linear stability analysis

It is known that the spinodal decomposition (instability) regime starts at the value of $h$ corresponding to the minimum of $\tilde{\Pi}(\tilde{h})$ [22]. In our dimensionless notation, $\tilde{h}^* = h^*/a$, the minimum is located at

$$\tilde{h}^* = [(2 - \beta) + \sqrt{(\beta - 2)^2 + 9\beta}]/3. \tag{16}$$

Thus, the instability occurs for $\tilde{h} > \tilde{h}^*$, where $\tilde{\Pi}(\tilde{h})$ is negative and its derivative is positive. This is shown by the standard linear stability analysis [18, 19], as follows.

We apply a small-amplitude perturbation ($\varepsilon$) at a given wavenumber $\tilde{k}$ and imaginary frequency $\tilde{\omega}$ (both dimensionless), i.e., $\tilde{h}(\tilde{x}, \tilde{y}, \tilde{t}) = \tilde{h}_0(1 + \varepsilon\, e^{i\tilde{\mathbf{k}}\cdot\tilde{\mathbf{r}}} e^{-\tilde{\omega}\tilde{t}})$, where $\tilde{h}_0$ is the initial uniform film height. By expanding to first order we obtain

$$\tilde{\omega}(\tilde{k}) = \tilde{h}_0^3 \tilde{k}^2 \left(\tilde{k}^2 - \tilde{k}_c^2\right), \tag{17}$$

where the critical wavenumber, $\tilde{k}_c$, is defined by:

$$\tilde{k}_c^2 = \frac{\gamma^2}{\tilde{h}_0^4}\left(\frac{\tilde{h}_0 - 1}{\tilde{h}_0 + \beta}\right)\left[3 - \frac{\tilde{h}_0(1 + \beta)}{(\tilde{h}_0 - 1)(\tilde{h}_0 + \beta)}\right] = \frac{d\tilde{\Pi}(\tilde{h}_0)}{d\tilde{h}_0}. \tag{18}$$

According to (17), an unstable mode exists as long as $\tilde{k}_c^2 > 0$. From (18), one can show that this occurs for $\tilde{h}_0 > \tilde{h}^*$, where $\tilde{h}^*$ is defined in (16). Thus, films thicker than $\tilde{h}^*$ are unstable. An instability occurs for wavenumbers where $\tilde{k} < \tilde{k}_c$. The fastest growing mode is the one that has the largest $(-\tilde{\omega})$, which corresponds to the wavenumber $\tilde{k}_m = \tilde{k}_c/\sqrt{2}$. This maximum instability growth rate is $|\omega(\tilde{k}_m)| = \tilde{h}_0^3 \tilde{k}_m^4$, which leads to the time constant $\tilde{\tau}_m = (\tilde{h}_0^3 \tilde{k}_m^4)^{-1}$, meaning that the perturbation grows as $\sim e^{\tilde{t}/\tilde{\tau}_m}$. The spinodal wavelength (corresponding to the fastest growing mode) is

$$\tilde{\lambda}_m = 2\pi/\tilde{k}_m = 2\pi\sqrt{2}/\tilde{k}_c. \tag{19}$$

For values $\tilde{h}_0 \gg \tilde{h}^*$, one extracts the asymptotic behavior

$$\tilde{\lambda}_m \sim g_1\, \tilde{h}_0^2, \qquad \tilde{\tau}_m \sim g_2\, \tilde{h}_0^5, \quad \text{for } \tilde{h}_0 \gg 1, \tag{20a}$$

where

$$g_1 = \frac{2\pi\sqrt{2}}{\gamma\sqrt{3}}, \qquad g_2 = \frac{4}{9\gamma^4}. \tag{20b}$$

**Table 1.** Time and length scales for different elements, computed from equations (13)–(15) for $\gamma = 5.13$. Here $a$ represents the scale of the height $h$, and $\xi$ is the scale in the planar ($x$ and $y$) direction as introduced in equation (10), and $\tau$ is the time scale. The quantity $\beta$ is defined in (9).

| Atom | $a$ (Å) | $\xi$ ($\mu$m) | $\tau$ (s) | $\beta$ |
|---|---|---|---|---|
| $N_2$ | 36 | 0.210 | $2.77 \times 10^{-3}$ | 0.37 |
| $H_2$ | 114 | 2.11 | 0.271 | 0.16 |
| He | 301 | 13.9 | 52.3 | 0.073 |

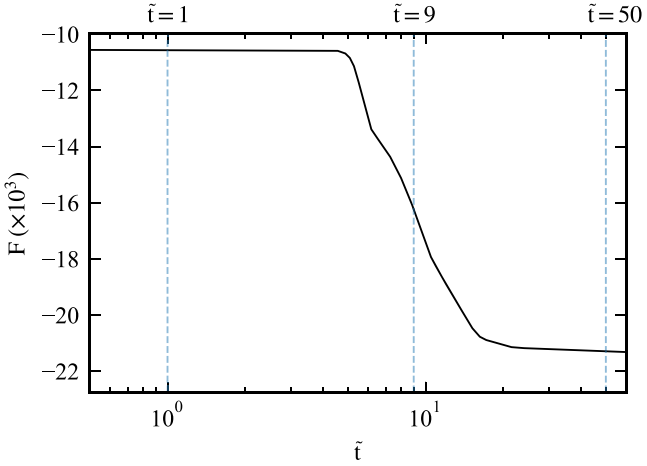


**Figure 6.** Evolution of the free energy equation (24) with time for the $N_2$ film, obtained by FEM. Total value of the free energy depends on the area of the system ($A = 100\xi \times 100\xi$).

The choice $\gamma = 5.13$ results in $g_1 = 1$, which leads to a simple form of the asymptotic dependence of the most unstable wavelength on the film height (in non-dimensional units). We found this to be a convenient choice in the numerical simulations, but any other choice of $\gamma$ is also acceptable.

Plots of the spinodal wavelength (figure 3) and the spinodal growth time constant (figure 4) show divergence at the instability threshold and then increase as power laws for larger film heights. At the onset of instability, i.e., for $\tilde{h} \to \tilde{h}^* + 0$, the critical wavenumber is $\tilde{k}_c \sim (\tilde{h} - \tilde{h}^*)^{1/2}$, and therefore the most unstable wavelength diverges as $\tilde{\lambda}_m \sim (\tilde{h} - \tilde{h}^*)^{-1/2}$. The time scale of the instability, $\tilde{\tau}_m \sim (\tilde{h} - \tilde{h}^*)^{-2}$, diverges even more strongly than the wavelength.

In figures 3 and 4 we present these values $\tilde{\lambda}_m$ and $\tilde{\tau}_m$ along with the corresponding quantities obtained from numerical simulations (see section 4) by calculating a radially averaged 2D Fourier transform of $\tilde{h}(x, y)$ at each time step and identifying the fastest growing modes. We find excellent agreement between the results from linear stability analysis and numerical simulations across all values of the initial heights tested. The dependence on the parameter $\beta$, which varies with the type of liquid, is relatively weak, practically non-existent for $\lambda_m$ and somewhat more pronounced for $\tau_m$.

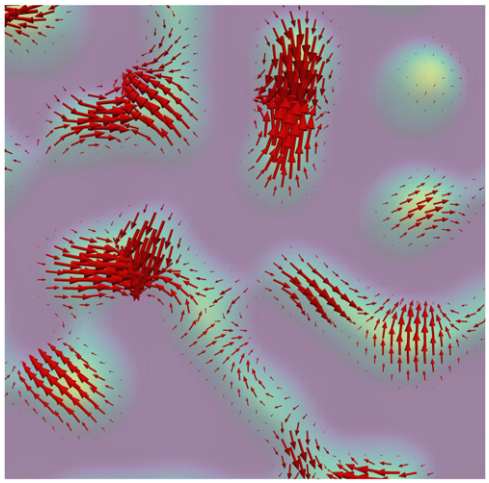

**Figure 7.** Close-up of the flux vector field ($\tilde{\mathbf{J}}$, red arrows) for the $N_2$ FEM simulation shown in figure 5 (center panel). Arrow sizes are scaled by the magnitude of the flux vector at a particular $x$–$y$ location. Note how the flux vector field depicts different types of motions within the fluid including the translational motion of large features as well as the merging of neighboring ones (regions with high density of arrows). Height data shown in the background where purple/dark colors correspond to values of $\tilde{h} \approx 1$ and yellow/light green colors to $\tilde{h} \leqslant 9$.

## 4. Numerical simulations of spinodal de-wetting

### *4.1. Finite element simulations*

To perform numerical simulations of equation (12), we first rewrite it in the form of a continuity equation:

$$\partial_{\tilde{t}} \tilde{h} = \tilde{\nabla} \cdot \tilde{\mathbf{J}} \tag{21}$$

where

$$\tilde{\mathbf{J}} = \tilde{h}^3 \tilde{\nabla} \nu(\tilde{h}) \tag{22}$$

is the dimensionless particle flux vector field, and we have defined for convenience the quantity $\nu(\tilde{h}) = -\Delta\tilde{h} - \tilde{\Pi}(\tilde{h})$. To guarantee that the mass of the liquid over a given area of the substrate is conserved, we impose the following zero-flux boundary conditions:

$$\tilde{\nabla}\nu \cdot \hat{n} = 0 \quad \text{on } C; \tag{23}$$

here, curve $C$ is the boundary of the given area and $\hat{n}$ is the unit normal vector to the boundary. Indeed, integrating over the given area and applying the 2D version of the divergence theorem, we obtain $\partial_t \int \tilde{h} \mathrm{d}\tilde{S} = \int_C \tilde{h}^3 (\tilde{\nabla}\nu \cdot \hat{n}) \mathrm{d}l = 0$, where the last equation follows from (23). (The mass with all units restored is $n_{\text{liquid}} \int h \mathrm{d}S$, where $n_{\text{liquid}}$ is the liquid density.)

Numerical simulations of equations (21) and (22) were performed in Python with the FEniCS automated FEM package [38–40]. A standard Lagrange finite-element basis was used to solve these equations variationally [39]. Time integration was performed using the standard finite difference Crank–Nicolson method [41]. Sufficiently small time steps

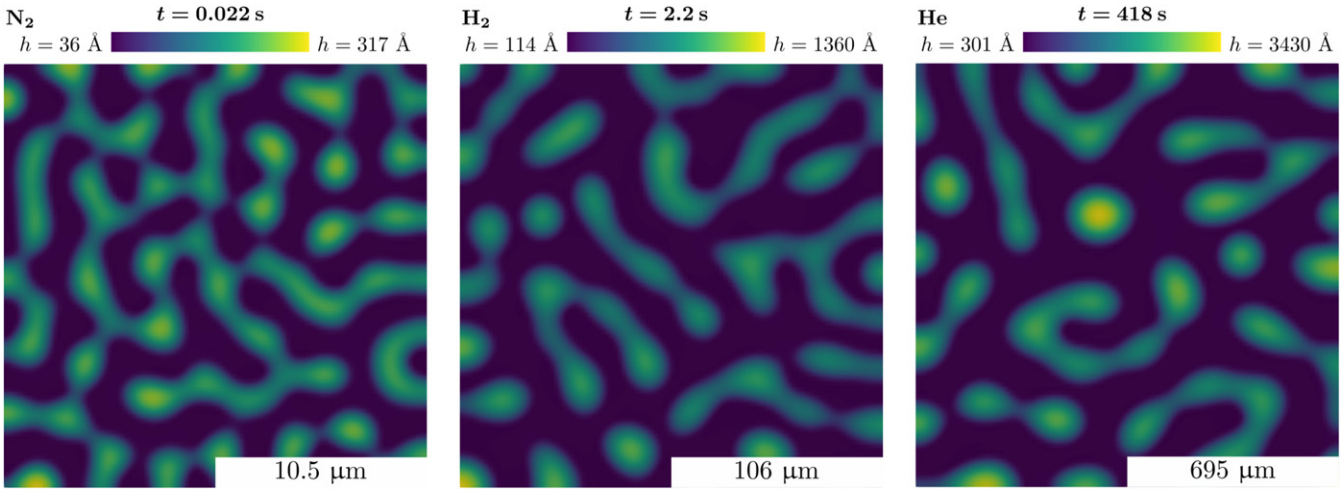


**Figure 8.** Comparison of spinodal de-wetting patterns observed in FEM simulations of liquids on graphene for $N_2$ (left panel), $H_2$ (center panel), and He (right panel). For all three cases shown, the dimensionless parameters are the same ($\tilde{h}_0 = 3.0$, $t = 8\tau$, and $100\xi$ simulation size) except for $\beta$ (see table 1). While the patterns are qualitatively similar regardless of the liquid, the length and time scales are vastly different as discussed in the main text.

were chosen in order to facilitate convergence of the FEM solvers depending on the parameters for each species (see table 1) and film thickness values. Numerical accuracy was monitored by checking conservation of total mass at each time step ($\mathrm{d}M/M_{\mathrm{total}} < 10^{-14}$).

The starting condition for all simulations corresponded to the spatially uniform film of thickness ($\tilde{h}_0$) with very small random variations ($<\tilde{h}_0 \times 10^{-5}$). Neumann boundary conditions were applied at the edges of the simulation box (equation (23)). Analysis of the FEM simulations was performed with the NumPy and SciPy libraries [42, 43].

### *4.2. Time evolution of spinodal de-wetting patterns*

The spinodal de-wetting patterns for $N_2$ (taken as an example) with $\tilde{h}_0 = 3$ obtained from numerical simulations are presented in figure 5 for three different times (corresponding to the free energy evolution in figure 6). These show the characteristic spinodal surface patterns as time increases, culminating in large height fluctuations at late times. For $N_2$ (figure 5), the observed distance between features at the initial/intermediate stages is $\sim$1 $\mu$m in agreement with the spinodal wavelength values shown in figure 3 (in units of the length scale $\xi \approx 0.2$ $\mu$m, see table 1).

The observed time evolution of the liquid film can be further characterized by considering the free energy:

$$F = \iint \left\{ \frac{1}{2}|\nabla\tilde{h}|^2 + U(\tilde{h}) \right\} \mathrm{d}\tilde{x}\mathrm{d}\tilde{y}, \tag{24}$$

where the potential energy $U(\tilde{h})$ is defined as $\partial U/\partial\tilde{h} = -\tilde{\Pi}(\tilde{h})$,

$$U(\tilde{h}) = \frac{\gamma^2}{2\beta}\frac{1}{\tilde{h}^2} - \frac{\gamma^2(1+\beta)}{\beta^2}\frac{1}{\tilde{h}} + \frac{\gamma^2(1+\beta)}{\beta^3}\ln\left(1+\frac{\beta}{\tilde{h}}\right). \tag{25}$$

The free energy in equation (24) decreases with time and is constant only on stable stationary solutions if/when they exist: $\frac{\mathrm{d}F}{\mathrm{d}t} \leqslant 0$ [22]. Values of the free energy for the $N_2$ numerical simulation are shown in figure 6. During the initial time evolution, $\tilde{t} < 5$, the small-scale fluctuations of the film thickness are reflected in the approximately constant energy. At intermediate times, $5 < \tilde{t} < 20$, the energy rapidly changes as the spinodal fluctuations grow macroscopically and well-defined ridges of material accumulate above a nearly uniform film surface of thickness $\tilde{h} \gtrsim 1$ (see caption for figure 5). At larger (dimensionless) times, $\tilde{t} > 20$, the energy enters a slowly changing regime as the ridges merge into isolated droplets that accumulate the excess liquid, surrounded by large areas of flat surface. The above stages of the film evolution follow a well-established sequence, for example as reported in [20] for a different physical system (different $\Pi(h)$).

The redistribution of mass in the process of de-wetting can be more clearly observed with the help of the flux vector, $\tilde{\mathbf{J}}$, as shown in figure 7. While the total mass is conserved, as discussed previously, there is significant flow toward regions of larger height, relative to the uniform value.

Having examined patterns at different times for $N_2$, we turn our attention to comparing the evolutions for different elements. The time and length scales for the three elements listed in table 1 are quite different. Namely, the time scale is the shortest for $N_2$ and longest for He; this results in the evolution of He being much slower than that of the other two liquids in physical units. For example, for the nondimensional height $\tilde{h}_0 = 3$, the spinodal growth time scale for He is $\tau_{\mathrm{m}} \sim 10$ s, while this time scale for $H_2$ and $N_2$ is $\sim 10^{-1}$ s and $10^{-3}$ s, respectively. Moreover, as shown in figure 8, the same *dimensionless* simulation time results in patterns corresponding to somewhat later stages of evolution for He than for $H_2$ and $N_2$. We hypothesize that this difference can be caused by the different values of $\beta$ for these three elements, because in all other respects their dimensionless equation (12) is identical. In the same figure, we can see that at the intermediate stage of the evolution, the characteristic size of the emerging 'ridges' approximately follows

the scale of the most unstable wavelength, whose values for the initial film thickness in question, $\tilde{h}_0 = 3$, are: $\lambda_m \sim 1$ $\mu$m (for $N_2$), $\lambda_m \sim 10$ $\mu$m (for $H_2$), and $\lambda_m \sim 100$ $\mu$m (for He). Recall from (20a) that $\tilde{\lambda}_m \propto \tilde{h}_0^2$. We also observe that as the initial thickness $\tilde{h}_0$ increases, the diameter of the droplets formed at the terminal stage of the evolution also increases, albeit slower than quadratically. This is consistent with similar observations in a different physical context [44].

## 5. Conclusions and outlook

This work predicts the existence of surface de-wetting patterns for light liquids on suspended graphene and investigates in detail the spatial and temporal scales that characterize those patterns. The first important step in the problem is the calculation of the disjoining pressure $\Pi(h)$, using the approach laid out in reference [13]. This function can be determined very accurately for various elements on graphene since the atomic parameters and graphene's polarization can be calculated with great accuracy. In fact, the general shape shown in figure 2 is quite universal and representative of numerous 2D materials such as members of the dichalcogenides family ($MoSe_2$, $MoS_2$, $WSe_2$, $WS_2$). For all of these, the film thickness $h^*$ at which spinodal de-wetting starts (for He liquid) is between 100 Å and 300 Å [13]. Applying additional perturbations to graphene itself, such as electronic (or hole) doping via external voltage, also affects $h^*$, generally increasing it [13]. Therefore spinodal patterns are possible for liquids on all of those materials as well, the main difference being in the various characteristic length and time-scales which are very material specific. We also point out that the most important physical assumption in our analysis leading to figure 2 and everything that follows is that graphene (or any of the other 2D materials) are in the suspended configuration, since only in this case a finite $h^*$ is predicted, whereas the presence of an additional (bulk) substrate creates too much VDW attraction and sends $h^*$ to infinity. The possibility of suspended configurations is a unique feature of 2D materials.

An advantage of studying light liquids, as we have done in this work, is that their spinodal de-wetting characteristics can be predicted theoretically very accurately, in the relatively low-temperature regime where liquid phases exist. For complex liquids, including liquid metals, this would not be a simple task. Additional real-world factors such as, for example, bending of suspended graphene sheets (or other 2D materials) should also in principle be taken into account in the calculation of VDW interactions.

The spinodal de-wetting patterns observed numerically (see figure 5) for various liquids on graphene are quite universal in shape and time evolution when written in dimensionless form. The main difference is in the time and length scales for different elements (table 1 and figures 3 and 4). We also found that the spinodal wavelengths, and subsequently the spatial scales of the emerging patterns (ridges and droplets), are generally quite long compared to the critical film thickness for spinodal onset (which is up to several hundred Å), and range between 1 $\mu$m and 100 $\mu$m depending on the liquid.

While in this work we considered the instability of the film surface with respect to small initial perturbations, it should be noted that different dynamics may result, for certain ranges of the initial film thickness, when the film is subject to finite perturbations to its shape. A study of the resulting metastable and 'nucleation-dominated' regimes (see, e.g., [31, 45–47]) of a film's surface evolution is outside the scope of this paper.

We hope this work stimulates further theoretical and experimental research related to the physics of spinodal de-wetting on 2D atomically thin crystals, especially since this phenomenon appears to be a universal feature for this class of materials. We emphasize again the most important advantages of 2D materials, such as graphene:

—The spinodal de-wetting instability is a generic phenomenon in such materials and occurs spontaneously at the instability onset $h^*$ due to the fact that 2D structures are weak adsorbers, i.e., their VDW potential is not strong enough to maintain a film with uniform thickness in excess of $h > h^*$.

—Given that 2D material parameters are known with great accuracy, the spinodal de-wetting onset $h^*$ and the evolution of the spinodal de-wetting patterns can be reliably predicted for liquids with well-established polarization characteristics.

—Because graphene and 2D materials can be also manipulated via external factors such as carrier doping, strain, etc, this can be used as a guiding principle for creation and control of de-wetting patterns. For example a range of values $h^*$ was found in [13] for graphene and other 2D materials, such as monolayer dichalcogenides, which could lead to applications in micro-pattern design [26].

## Acknowledgments

We are grateful to Adrian Del Maestro and Peter Taborek for numerous stimulating discussions related to the physics of wetting and wetting instabilities. JMV, TIL and VNK gratefully acknowledge financial support from NASA Grant No. 80NSSC19M0143.

## Data availability statement

All data that support the findings of this study are included within the article (and any supplementary files).

## Appendix A. Details of disjoining pressure calculations for light atoms on graphene

Here we summarize the results of calculations related to the determination of the disjoining pressure $\Pi(h)$, equation (1), which is used to extract the relevant parameters for different atoms, equations (3)–(5). The form of equation (1) follows from the microscopic DLP theory [33, 34], when applied to 2D materials, which describes VDW interactions in anisotropic (layered) situations such as liquids on solid substrates

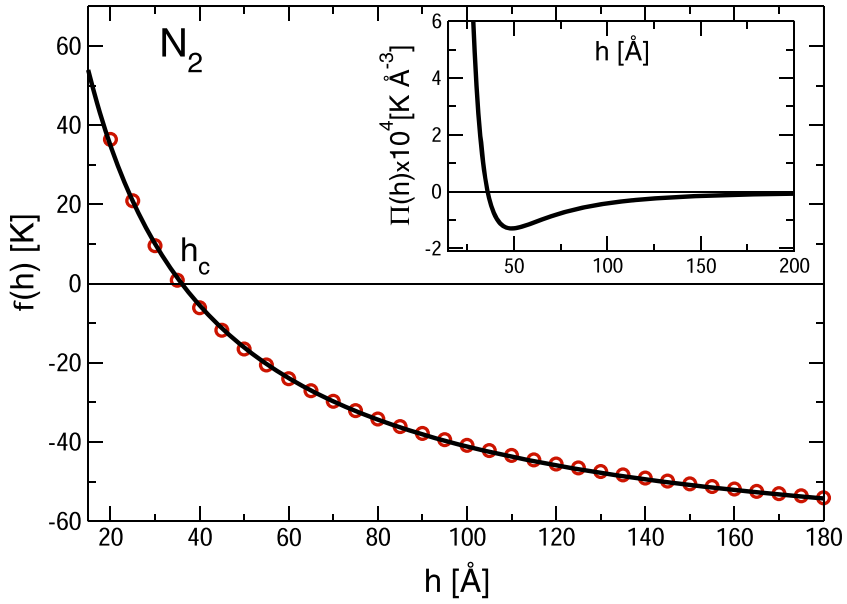


**Figure 9.** The function $f(h)$, defined so that the disjoining pressure has the form $\Pi(h) = f(h)/h^3$. For $N_2$, $f(h)$ is calculated by evaluating the microscopic expressions equations (A1) and (A7), and is shown as a solid line in the main panel. The red circles represent a fit to the form $f(h) = -|\Pi_0| + \frac{\Pi_1}{h+L}$ (as in equation (1)), with $|\Pi_0| = 72.8$ K, $\Pi_1 = 3592$ KÅ, $L = 13.3$ Å. These are the values used in the main text, equation (3). Inset: the full function $\Pi(h) = f(h)/h^3$.

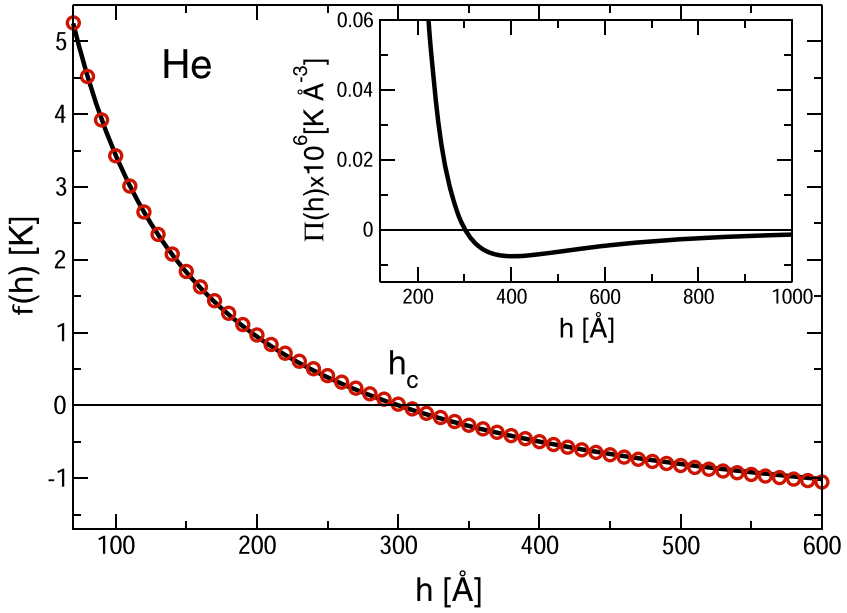


**Figure 10.** Results for He, following the same procedure as in figure 9. With $\Pi(h) = f(h)/h^3$, the main panel shows the exact numerical evaluation of $f(h)$, solid line. The red circles represent a fit to the form $f(h) = -|\Pi_0| + \frac{\Pi_1}{h+L}$ (as in equation (1)), with $|\Pi_0| = 2.09$ K, $\Pi_1 = 676$ KÅ, $L = 22.1$ Å. These are the values used in the main text, equation (5). Inset: the full function $\Pi(h) = f(h)/h^3$. Notice the different scales on this graph compared to figure 9.

[4, 33, 34]. The standard calculations and typical applications assume a bulk (usually dielectric) substrate with a liquid formed on top, in equilibrium with its vapor. In [13] one of us and collaborators extended the standard theory to several physical situations involving 2D materials, and in particular to the case when a 2D semimetal, such a graphene, is used as a substrate instead of a bulk material (as shown in figure 1). We refer the reader to [13] for details of calculations.

The ground state energy of this system can be written as (we set $\hbar = 1$):

$$U_{\rm vdw}(h) = \frac{1}{(2\pi)^3}\int {\rm d}^2\mathbf{q}\int_0^\infty {\rm d}\omega(\mathcal{U}_{\rm d}(q,{\rm i}\omega) + \mathcal{U}_{\rm g}(q,{\rm i}\omega)), \tag{A1}$$

where $\mathcal{U}_{\rm d}(q,{\rm i}\omega)$ describes the liquid with dielectric function $\varepsilon({\rm i}\omega)$ and thickness $h$, without a substrate and with liquid vapor

on top (taken as vacuum, dielectric constant equal to one),

$$\mathcal{U}_{\rm d}(q,{\rm i}\omega)=\frac{(\varepsilon({\rm i}\omega)-1)(1-\varepsilon({\rm i}\omega))}{(\varepsilon({\rm i}\omega)+1)(1+\varepsilon({\rm i}\omega))}{\rm e}^{-2qh}, \qquad \text{(A2)}$$

and $\mathcal{U}_{\rm g}(q,{\rm i}\omega)$ is the graphene substrate–liquid interaction part:

$$\mathcal{U}_{\rm g}(q,{\rm i}\omega)=\frac{\left(\frac{-4\pi{\rm e}^2\chi(q,{\rm i}\omega)}{q(\varepsilon({\rm i}\omega)+1)}\right)\left(\frac{\varepsilon({\rm i}\omega)-1}{\varepsilon({\rm i}\omega)+1}\right)\left(\frac{2\varepsilon({\rm i}\omega)}{\varepsilon({\rm i}\omega)+1}\right)}{1-\frac{4\pi{\rm e}^2\chi(q,{\rm i}\omega)}{q(\varepsilon({\rm i}\omega)+1)}}{\rm e}^{-2qh}. \qquad \text{(A3)}$$

Equations (A2) and (A3) follow from more general expressions (describing different geometries) derived in [13]. Here $q=|\mathbf{q}|$ is the magnitude of the in-plane momentum and $\chi(q,{\rm i}\omega)$ is graphene's polarization function which is known to be [12]:

$$\chi(q,{\rm i}\omega)=-\frac{1}{4}\frac{q^2}{\sqrt{v^2q^2+\omega^2}}, \qquad \text{(A4)}$$

where $v=6.6$ eV Å is the velocity of the Dirac quasiparticles. We have modified somewhat the notations used in [13] in order to achieve consistency with the symbols across the present paper.

It should be emphasized that equation (A1) describes any 2D material (not only graphene), with a dynamical polarization $\chi(q,{\rm i}\omega)$, in the suspended configuration. This allows one to compute the spinodal instability threshold $h^*$ and indeed the function $\Pi(h)$ with high accuracy. We also note: (1) relativistic effects are negligible in the range of distances of interest to us (up to hundreds of Å) [10, 13]. (2) The energy in equation (A1) is written at zero temperature since finite-temperature effects in the VDW energy expression are negligibly small in the range of distances studied (as shown in reference [13] (supplementary material)). Of course the various atom-related characteristics have to be used in the temperature regime where the liquid phase is stable, as in section 3.2.

Several additional comments are in order. First, the fact that $U_{\rm vdw}(h)$ involves integration over the imaginary frequency axis is a common mathematical feature when writing the ground state energy of the system [4, 33, 34]. Second, notice that $\mathcal{U}_{\rm d}(q,{\rm i}\omega)<0$, while $\mathcal{U}_{\rm g}(q,{\rm i}\omega)>0$ (since we always have $\varepsilon>1$, which reflects screening). This will be important in what follows. Third, the terms $\mathcal{U}_{\rm d}$ and $\mathcal{U}_{\rm g}$ depend on $h$ only through the exponential factor. The nontrivial dependence of $U_{\rm vdw}(h)$ on $h$ arises after integration over the momentum $\mathbf{q}$. Notice also that graphene's polarization $\chi(q,{\rm i}\omega)$ has a pronounced momentum dependence which reflects the motion of graphene's quasiparticles.

For completeness we also summarize the dielectric functions of the three liquids used in this work, as described in [13], which cites additional literature. For Helium the dynamical dielectric constant is

$$\varepsilon({\rm i}\omega)=1+4\pi n_{\rm He}\alpha({\rm i}\omega), \qquad \alpha({\rm i}\omega)=\frac{\alpha_{\rm He}}{1+(\omega/\omega_{\rm He})^2}, \qquad \text{(A5)}$$

where the density $n_{\rm He}=2.12\times10^{-2}$ Å$^{-3}$, the static polarizability $\alpha_{\rm He}=1.38$ a.u., and the characteristic oscillator frequency $\omega_{\rm He}=27.2$ eV. The atomic unit of polarizability is defined as 1 a.u. $=0.148$Å$^3$. For nitrogen and hydrogen, which have densities comparable to helium but significantly larger polarizabilities, more accurate formulas based on the Clausius–Mossotti relation are typically used:

$$\varepsilon({\rm i}\omega)=1+\frac{4\pi n_{\rm A}\alpha({\rm i}\omega)}{1-\frac{4\pi}{3}n_{\rm A}\alpha({\rm i}\omega)}, \quad A={\rm N_2},\ {\rm H_2} \qquad \text{(A6)}$$

The dynamical polarizability $\alpha({\rm i}\omega)$ is defined as in equation (A5), i.e. has the form $\alpha({\rm i}\omega)=\frac{\alpha_{\rm A}}{1+(\omega/\omega_{\rm A})^2}$. For $H_2$ the parameters are: $n_{\rm H_2}=2.04\times10^{-2}$Å$^{-3}$, $\alpha_{\rm H_2}=5.44$ a.u., $\omega_{\rm H_2}=14.09$ eV. For $N_2$: $n_{\rm N_2}=1.73\times10^{-2}$Å$^{-3}$, $\alpha_{\rm N_2}=11.74$ a.u., $\omega_{\rm N_2}=19.32$ eV.

The VDW energy defined in equation (A1) has physical dimensions of energy per unit area. The disjoining pressure is defined as:

$$\Pi(h)=-\frac{\partial U_{\rm vdw}(h)}{\partial h}, \qquad \text{(A7)}$$

and describes the effective force per unit area between the two boundaries of the system (liquid–vapor and liquid–graphene). It is clear that the part of $\Pi(h)$ which comes from $\mathcal{U}_{\rm g}(q,{\rm i}\omega)>0$ leads to positive pressure, i.e. favors film growth, while the part associated with $\mathcal{U}_{\rm d}(q,{\rm i}\omega)<0$ is always negative, i.e. favors an instability. It is the competition between these two terms that leads to the spinodal de-wetting instability phenomenon.

Finally we return to the way we determine the all-important functional form of $\Pi(h)$, equation (1), which follows from the microscopic expressions equations (A1) and (A7). First we present the following qualitative considerations. As mentioned previously, it is useful to consider the contributions of the $\mathcal{U}_{\rm d,g}(q,{\rm i}\omega)$ terms separately. The (attractive) $\mathcal{U}_{\rm d}$ part clearly leads to dependence of the form $\Pi(h)\sim-\frac{1}{h^3}$ which follows from counting powers of momenta in the integrals. The (repulsive) $\mathcal{U}_{\rm g}$ part, however, exhibits a higher power due to the presence of graphene's polarization $\chi(q,{\rm i}\omega)$. Since at intermediate frequencies, which are dominant in the integration, the dependence of $\chi(q,{\rm i}\omega)$ on momentum is quadratic for low momenta, this leads to $\Pi(h)\sim1/h^4$. The exact way this crossover happens has to be determined numerically, by evaluating the expression equations (A1) and (A7), which can be done with high accuracy. In figure 9 we show the way this procedure works for $N_2$ and, as another example, in figure 10 we present the results for He. Most importantly, we can conclude that the functional form of $\Pi(h)$, equation (1), used in the main text, is very accurate.

## ORCID iDs

Juan M Vanegas https://orcid.org/0000-0003-1381-1649
Valeri N Kotov https://orcid.org/0000-0002-4592-6232

## References

[1] Castro Neto A H, Guinea F, Peres N M R, Novoselov K S and Geim A K 2009 *Rev. Mod. Phys.* **81** 109
[2] Geim A K and Grigorieva I V 2013 *Nature* **499** 419
[3] Novoselov K S, Mishchenko A, Carvalho A and Castro Neto A H 2016 *Science* **353** 461

[4] Israelachvili J N 2011 *Intermolecular and Surface Forces* (New York: Academic)
[5] De Gennes P G 1985 *Rev. Mod. Phys.* **57** 827
[6] Bonn D, Eggers J, Indekeu J, Meunier J and Rolley E 2009 *Rev. Mod. Phys.* **81** 739
[7] Craster R V and Matar O K 2009 *Rev. Mod. Phys.* **81** 1131
[8] Oron A, Davis S H and Bankoff S G 1997 *Rev. Mod. Phys.* **69** 931
[9] Sharma A, Harnish P, Sylvester A, Kotov V N and Neto A H C 2014 *Phys. Rev.* B **89** 235425
[10] Nichols N S, Del Maestro A, Wexler C and Kotov V N 2016 *Phys. Rev.* B **93** 205412
[11] Amorim B *et al* 2016 *Phys. Rep.* **617** 1
[12] Kotov V N, Uchoa B, Pereira V M, Guinea F and Castro Neto A H 2012 *Rev. Mod. Phys.* **84** 1067
[13] Sengupta S, Nichols N S, Del Maestro A and Kotov V N 2018 *Phys. Rev. Lett.* **120** 236802
[14] Sun P Z *et al* 2020 *Nature* **579** 229
[15] Berry V 2013 *Carbon* **62** 1
[16] Nair R R, Wu H A, Jayaram P N, Grigorieva I V and Geim A K 2012 *Science* **335** 442
[17] Bunch J S, Verbridge S S, Alden J S, van der Zande A M, Parpia J M, Craighead H G and McEuen P L 2008 *Nano Lett.* **8** 2458
[18] Ruckenstein E and Jain R K 1974 *J. Chem. Soc., Faraday Trans. II* **70** 132
[19] Vrij A 1966 *Discuss. Faraday Soc.* **42** 23
[20] Sharma A and Khanna R 1998 *Phys. Rev. Lett.* **81** 3463
[21] Reiter G, Sharma A, Casoli A, David M-O, Khanna R and Auroy P 1999 *Langmuir* **15** 2551
[22] Mitlin V S 1993 *J. Colloid Interface Sci.* **156** 491
[23] Xie R, Karim A, Douglas J F, Han C C and Weiss R A 1998 *Phys. Rev. Lett.* **81** 1251
[24] Alizadeh Pahlavan A, Cueto-Felgueroso L, Hosoi A E, McKinley G H and Juanes R 2018 *J. Fluid Mech.* **845** 642
[25] Mitlin V S and Petviashvili N V 1994 *Phys. Lett.* A **192** 323
[26] Gentili D, Foschi G, Valle F, Cavallini M and Biscarini F 2012 *Chem. Soc. Rev.* **41** 4430
[27] Rauscher M, Blossey R, Münch A and Wagner B 2008 *Langmuir* **24** 12290
[28] Seemann R, Herminghaus S and Jacobs K 2001 *Phys. Rev. Lett.* **86** 5534
[29] Seemann R, Herminghaus S and Jacobs K 2001 *J. Phys.: Condens. Matter* **13** 4925
[30] Seemann R, Herminghaus S, Neto C, Schlagowski S, Podzimek D, Konrad R, Mantz H and Jacobs K 2005 *J. Phys.: Condens. Matter* **17** S267
[31] Thiele U 2007 *Thin Films of Soft Matter* (*CISM International Centre for Mechanical Sciences* vol 490) ed S Kalliadasis and U Thiele (Berlin: Springer) pp 25–94
[32] Cahn J W 1965 *J. Chem. Phys.* **42** 93
[33] Dzyaloshinskii I E, Lifshitz E M and Pitaevskii L P 1961 *Adv. Phys.* **10** 165
[34] Lifshitz E M and Pitaevskii L P 1980 *Statistical Physics, Part 2* (Oxford: Pergamon)
[35] Panella V, Chiarello R and Krim J 1996 *Phys. Rev. Lett.* **76** 3606
[36] Cheng E and Cole M W 1988 *Phys. Rev.* B **38** 987
[37] Linstrom P J and Mallard W G (ed) 2020 *NIST Chemistry WebBook, NIST Standard Reference Database Number 69* (Gaithersburg, MD: National Institute of Standards and Technology) (https://doi.org/10.18434/T4D303)
[38] Alnæs M S *et al* 2015 The FEniCS Project Version 1.5 *Arch. Num. Softw.* **3** 9–23
[39] Logg A *et al* 2012 *Automated Solution of Differential Equations by the Finite Element Method* (Berlin: Springer)
[40] Logg A and Wells G N 2010 *ACM T. Math. Softw.* **37** 2
[41] Crank J and Nicolson P 1947 *Math. Proc. Camb. Phil. Soc.* **43** 50
[42] Harris C R *et al* 2020 *Nature* **585** 357
[43] Virtanen P *et al* 2020 *Nat. Methods* **17** 261
[44] Sharma A and Reiter G 1996 *J. Colloid Interface Sci.* **178** 383
[45] Thiele U, Velarde M G and Neuffer K 2001 *Phys. Rev. Lett.* **87** 016104
[46] Becker J, Grün G, Seemann R, Mantz H, Jacobs K, Mecke K R and Blossey R 2003 *Nat. Mater.* **2** 59
[47] Sharma A 2003 *Eur. Phys. J.* E **12** 397